Available online at www.sciencedirect.com

ScienceDirect

Procedia Structural Integrity 47 (2023) 370–382

Structural Integrity Procedia

www.elsevier.com/locate/procedia

27th International Conference on Fracture and Structural Integrity (IGF27)

Tensile behaviour of a hot work tool steel manufactured via Laser Powder Bed Fusion: effect of an innovative high pressure heat treatment

Mattia Zanni[a]*, Alessandro Morri[a], Simone Messieri[b], Lorella Ceschini[a]

[a]*Department of Industrial Engineering (DIN), Alma Mater Studiorum, University of Bologna, Viale Risorgimento 4, 40136 Bologna, Italy*
[b]*Ducati Motor Holding, Via Cavalieri Ducati Antonio 3, 40132 Bologna, Italy*

Abstract

The combination of outstanding mechanical strength of tool steels and design freedom ensured by Additive Manufacturing (AM) processes is of a great interest for automotive applications. However, AM techniques produce peculiar defects, which affect the resulting mechanical behavior. For this reason, safety critical AM components are often subjected to *hot isostatic pressing* (HIP) to heal process defects. At the same time, tool steels require a proper quenching and tempering (QT) heat treatment to achieve high hardness and strength.

In the present work, the effect of an innovative *high pressure heat treatment* (HPHT) on the tensile properties of a hot work tool steel produced via Laser Powder Bed Fusion (LPBF) was investigated. LPBF samples were subjected to two post-process heat treatments: a conventional quenching and tempering heat treatment performed in vacuum (CHT), and an innovative HPHT combining HIP e QT in a single step, to heal LPBF defects and obtain high mechanical properties. HPHT featured the same quenching and tempering cycle of CHT but it was performed under high pressure in a HIP furnace and with longer austenitizing time to promote defect closure. Tensile tests indicated no significant effect on proof and tensile strength for HPHT compared to CHT, but a significant reduction of elongation after fracture. Fractographic analyses and fracture mechanics calculations indicated that both CHT and HPHT specimens failed via crack propagation from large LPBF defects when the stress intensity factor reached the material fracture toughness. Fractographic analyses indicated an incomplete defect closure during HPHT due to the presence of an oxide film on the inner surface of defects, thus justifying the same failure mechanism and strength of CHT samples. Instead, it was proposed that the reduced elongation could arise from coarsened grains due to the longer austenitizing.

* Corresponding author. Tel.: +39 051 93142
E-mail address: mattia.zanni2@unibo.it

2452-3216
10.1016/j.prostr.2023.07.087

Keywords: Hot Work Tool Steel; Laser Powder Bed Fusion; High Pressure Heat Treatment; Tensile Properties

1. Introduction

Hot work tool steels are special steels specifically designed for dies, tools and manufacturing equipment operating at high temperature, characterized by high hardness and strength and adequate toughness, also suitable for other critical mechanical components requiring high stiffness, hardness, tensile, fatigue strength and wear resistance (Ceschini et al. (2018)). Generally, they feature a medium-to-high C content and other alloying elements which maximize steel hardenability and promote carbides formation, such as Cr, Mo, V and W, and are produced via special metallurgical processes (such as Electro-Slag Remelting, Vacuum Arc Remelting and Powder Metallurgy) to ensure high cleanliness and homogeneity. The typical *Quenching and Tempering* (QT) heat treatment of tool steels consists of austenitizing, quenching and multiple tempering to produce a microstructure of tempered martensite and, often, alloying carbides. A sub-zero treatment can be performed after quenching to eliminate retained austenite and/or promote the precipitation of nanometric carbides, thus improving hardness, wear resistance and dimensional stability (Baldissera et al. (2008)).

Additive Manufacturing (AM) processes are gaining large interest in view of their enhanced design freedom compared to conventional techniques. Among them, the Laser Powder Bed Fusion (LPBF) technique is based on layer-by-layer manufacturing and involves the production of 3D complex parts by iteratively and selectively melting thin layers of metal powder (DebRoy et al. (2018), Hebert (2016)). Applied to tool steels, LPBF can potentially enable the manufacturing of optimized components with light weight and extremely high mechanical strength. However, all AM processes lead to the formation of peculiar defects which can severely impair mechanical properties. The most diffuse defects resulting from LPBF are gas porosities and *Lack of Fusion* defects. The former have a nearly spherical morphology and are due to gas entrapment during the melt pool solidification. The latter, instead, possess a highly irregular morphology, and originate from insufficient energy input. Defects reduce density and mechanical performance of LPBF components, locally intensifying the applied stress (Mostafaei et al. (2022), du Plessis et al. (2020)). To mitigate the detrimental effect of LPBF defects, a post-process *Hot Isostatic Pressing* (HIP), which is traditionally used to densify cast components or as a Powder Metallurgy technique, can be performed (Atkinson et al. (2000), Ahlfors (2020), du Plessis et al. (2020), Cegan et al. (2020), Asberg et al. (2019)). HIP involves the application of a high isostatic pressure (up to 200 MPa) using Ar as inert gas at high temperature (above 0.7 times the solidus temperature). Due to the limited cooling rates of traditional HIP furnaces, the heat treatment required to achieve the desired microstructure and mechanical properties (for example a QT treatment for tool steels) is traditionally performed after the HIP cycle, thus resulting in long treatment durations. However, modern HIP furnaces capable of rapid cooling enable the direct quenching from HIP conditions, and thus to integrate HIP and heat treatment in a single cycle which simultaneously aims at removing process defects and obtaining high mechanical properties, containing the overall cycle duration (Maistro et al. (2021), Krakhmalev et al. (2020), Qin et al. (2021), Sridar et al. (2020), Tocci et al. (2020)).

Based on the above, the present work investigates the effect of an innovative *High Pressure Heat Treatment* (HPHT), which combines HIP and QT in a single cycle, on the microstructure and tensile properties of a hot work tool steel manufactured via LPBF. For comparison, tensile properties were also characterized on samples subjected to the conventional QT heat treatment (hereafter indicated as CHT), performed in vacuum with no high pressure applied.

2. Experimental

Samples manufactured from the gas atomized feedstock powder with the nominal composition given in Table 1 were supplied by Böhler Edelstahl GmbH.

Table 1. Chemical composition (wt.%) of the feedstock powder and LPBF bars.

Composition (wt. %)	C	Cr	Mo	V	Si	Mn	Al	Fe
Nominal (feedstock powder)	0.50	4.50	3.00	0.55	0.20	0.25	-	Bal.
Effective (LPBF bars)	0.46	4.30	3.20	0.61	0.20	0.22	0.01	Bal.

Cylindrical bars (ø14 x 163 mm) were manufactured by LPBF using a Renishaw RenAM 500Q machine equipped with a pre-heated building plate (400 °C), under high-purity Ar atmosphere. Additional details on the LPBF process were not disclosed by the supplier due to industrial confidentiality. The effective composition of LPBF bars, evaluated according to ISO 14707:2021, is reported in Table 1. Bars were produced with their axis parallel to the vertical building direction (90° orientation), subjected to a stress relief annealing at 690 °C for 2 hours after the detachment from the building plate, and then to two different post-process heat treatments, indicated as CHT and HPHT (schematically depicted in Figure 1). CHT represents the conventional *quenching and multiple tempering* heat treatment composed of (i) austenitizing at 1070 °C for 20 min in vacuum (after a double preheating at 600 °C and 900 °C), (ii) quenching in nitrogen gas, (iii) double tempering at 510-520 °C for 150 min, (iv) sub-zero step at -80 °C for 180 min, and (v) final tempering at 520-530 °C for 150 min (v). Instead, HPHT is the innovative *high pressure heat treatment* which combines HIP and QT in a single treatment, i.e. a quenching and multiple tempering treatment performed under high pressure. HPHT featured the same quenching and tempering cycle but steps (i) to (iii) were performed under high pressure Ar, using a Quintus QIH60 furnace. In particular, step (i) (austenitizing, coincident with the HIP step) was performed under 200 MPa isostatic pressure and its duration was increased to 40 min, compared to 20 min in CHT, to promote material densification and closing of internal LPBF defects. Moreover, HPHT featured a quenching (step (ii)) under high pressure (between 200 and 90 MPa) with a cooling rate of 150 °C/min and step (iii) (1st and 2nd tempering) performed under 150 MPa isostatic pressure. Instead, steps (iv) and (v) (sub-zero step and 3rd tempering) were performed in the same conditions of CHT. Tensile specimens, with geometry shown in Figure 2, were machined from LPBF bars after heat treatment.

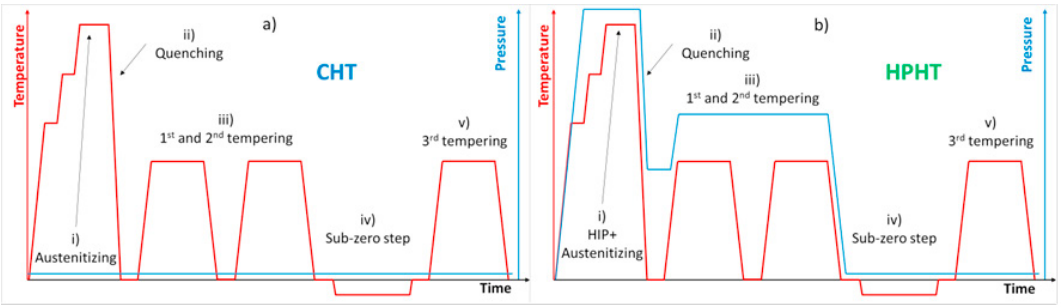

Fig. 1. Schematic representation of temperature and pressure cycles during CHT (a) and HPHT (b).

Tensile tests were performed according to ISO 6892-1:2019 for the determination of 0.2% proof strength ($R_{P0.2}$), ultimate tensile strength (UTS), elongation after fracture (A%), and area reduction after fracture (Z%). Four specimens were tested for both CHT and HPHT conditions. Vickers hardness (HV) indentations were performed according to ISO 6507-1:2018 using a 30 Kg load and 15 s duration. Fracture surfaces of tensile specimens were investigated using a Tescan Mira 3 Field Emission-Scanning Electron Microscope (SEM), equipped with X-ray Energy Dispersive Spectroscopy (EDS) to study the mechanisms of failure. Density and microstructural analyses were performed on samples extracted from the ø12 mm grip ends of tensile specimens in the transverse direction respect to the specimen axis. Samples were prepared following the standard procedure defined in ASTM E3-11 composed of hot mounting, grinding with abrasive papers up to 1200 grit and polishing with diamond suspension (9 µm, 3 µm, 1 µm). Low magnification images of polished sections were acquired using a Zeiss Axio Imager A.1M optical microscope (OM) and processed using the ImageJ v. 1.52a open-source software to perform defect analyses and calculate the density. Microstructural observations were performed using OM on sections chemically etched

with Picral (4 g picric acid, 100 mL ethanol) and SEM-EDS on sections etched with Vilella's reagent (1 g picric acid, 4 mL HCl, 96 mL ethanol).

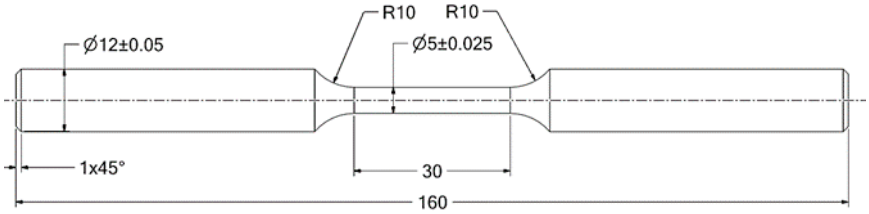

Fig. 2. Geometry and dimensions (mm) of tensile specimens.

3. Results and discussion

Image analysis indicated the beneficial effect in material densification of HPHT treatment, which resulted in a density of 99.97±0.02 % compared to 99.77±0.13 % of samples subjected to CHT. The different content of defects and their size distribution in samples subjected to CHT and HPHT are compared in Figure 3 and Figure 4, which respectively reports representative OM images of polished metallographic sections and the distribution of defects detected via image analysis. Despite the relatively high density, CHT samples exhibited a considerable number of defects with a relevant size ($\sqrt{area}$ of the largest detected defect equal to 86 μm) and circular morphology, consistent with *gas pores* resulting from gas entrapment in the melt during the LPBF process (Mostafaei et al. (2022), DebRoy et al. (2018)). A circular morphology was observed also for defects in HPHT samples. However, the number and size of defects detected in HPHT samples appeared considerably lower than in CHT ones, with no defect exceeding 36 μm, in agreement with density data. An extremely low amount of *Lack of Fusion* defects, with a complex, irregular morphology, was observed on polished sections.

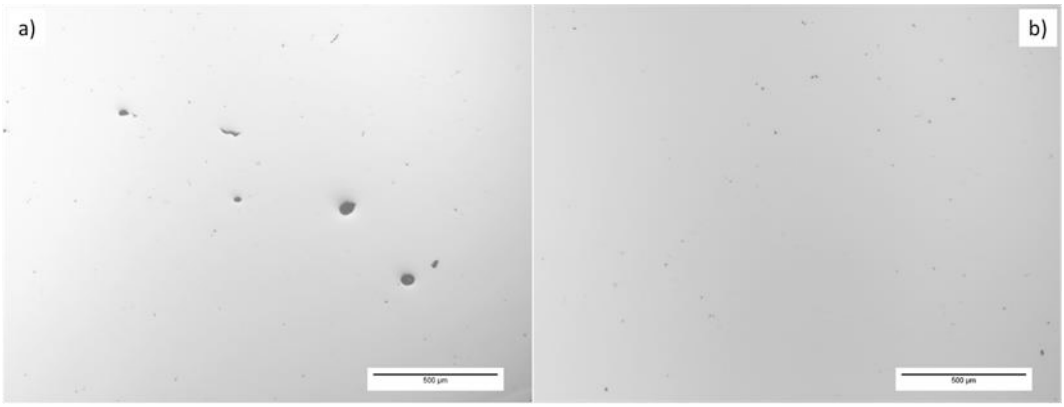

Fig. 3. Representative low magnification OM images acquired on polished sections of CHT (a) and HPHT (b) samples showing the different content of defects.

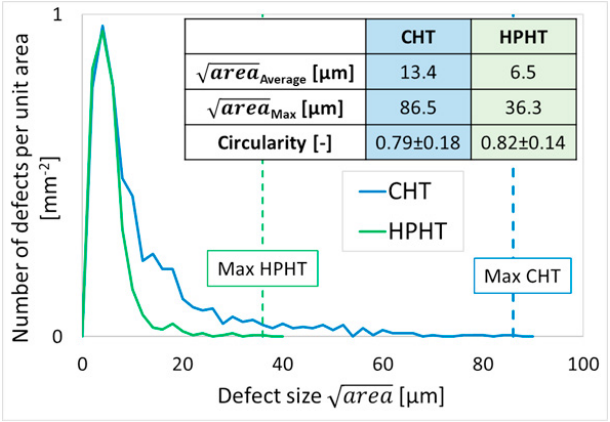

Fig. 4. Comparison between size distributions of defects detected via image analysis on polished metallographic sections of CHT and HPHT samples.

Table 2 summarizes the results of hardness and tensile tests. Compared to CHT, HPHT resulted in negligible variations of hardness HV, proof strength $R_{P0.2}$ and tensile strength UTS, but in a dramatical loss of ductility, as indicated by elongation A% and area reduction after fracture Z%. Therefore, no beneficial effect of HPHT on hardness and tensile properties was observed, despite the positive effect on density.

Table 2. Summary of hardness and tensile properties for samples subjected to CHT and HPHT treatments.

	HV	$R_{P0.2}$ [MPa]	UTS [MPa]	A% [%]	Z% [%]
CHT	665±5	1719±15	2280±3	3.4±0.5	6.9±0.4
HPHT	671±2	1739±9	2265±20	1.5±0.2	3.6±0.0
Δ%	+0.9 %	+1.2 %	-0.7 %	-56 %	-48 %

Figure 5 shows representative low magnification SEM images of fracture surfaces. Noticeably, neither CHT nor HPHT specimens exhibited the typical fracture appearance of ductile materials failed under monotonic tensile loads, i.e. a *cup-cone* fracture with a central fibrous zone created via *microvoids nucleation and coalescence* mechanism, responsible of dimples formation, surrounded by an external *shear-lip* zone. Instead, fracture surfaces indicated a failure mechanism consistent with unstable crack propagation, initiated from a single large discontinuity (hereafter indicated as *killer* defect) and propagated through the whole cross-section up to failure. An extremely limited *shear-lip* was observed, with lower width in HPHT specimens than in CHT ones, in agreement with the trend of Z%. In fact, *shear-lip* formation is strictly related to necking, i.e. the localization of plastic strains on a section at the maximum load, responsible for the reduction of cross-section area (McGarry (2021)). A similar fracture appearance for hot work tool steels manufactured via LPBF was reported also by Asberg et al. (2019), Lee et al. (2019) and Vilardell et al. (2021) and attributed to the presence of LPBF defects. At the microscale (Figure 6), both CHT and HPHT samples exhibited a mixed ductile-brittle fracture morphology on the whole surface (excluding the fully ductile *shear-lip*), composed of both dimples and cleavage facets and consistent with the supposed mechanism of unstable crack propagation. For comparison, the ESR counterpart of the steel, investigated by Ceschini et al. (2018), exhibited a fully ductile cup-cone fracture appearance, with no evidence of unstable crack propagation. Note that the mixed ductile-brittle appearance observed in tensile specimens in the present work is consistent with the morphology reported by Ceschini et al. (2018) for the final overload fracture region in fatigue specimens, which is typically originated via unstable crack propagation (Parrington (2021)).

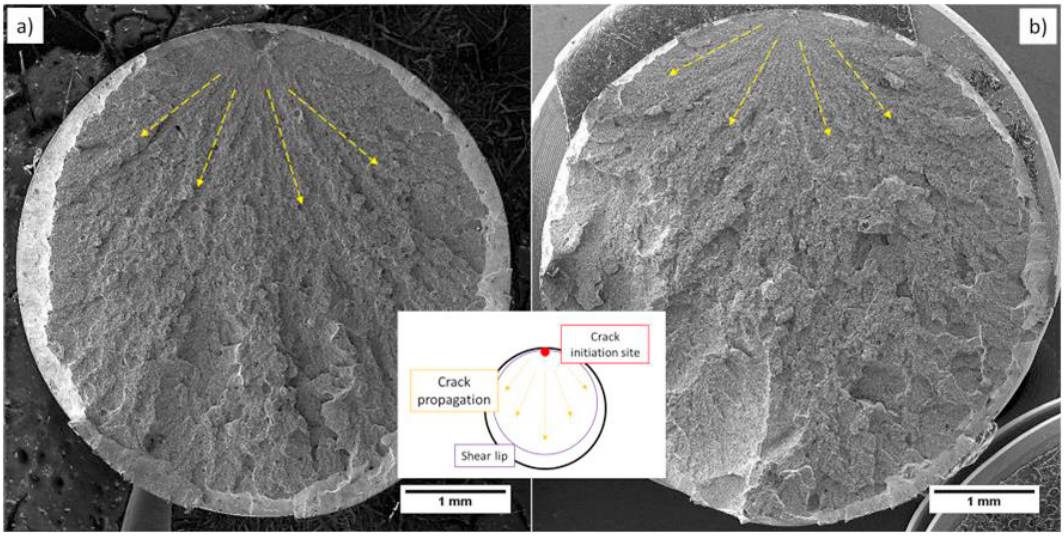

Fig. 5. Representative low magnification SEM images of the fracture surfaces of CHT (a) and HPHT (b) tensile samples; in the inset: proposed failure mechanism.

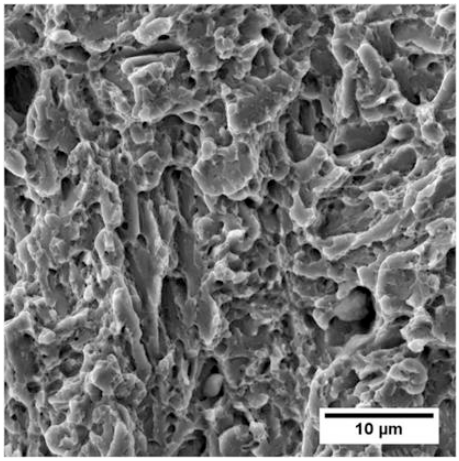

Fig. 6. Representative microscale fracture morphology of both CHT and HPHT samples.

To confirm the supposed unstable crack propagation failure mechanism, Linear-Elastic Fracture Mechanics (LEFM) were applied by calculating the mode I-stress intensity factor K_I at killer defects observed at the crack initiation sites on fracture surfaces, examples of which are reported in Figure 7. K_I was calculated using the formula

$$K_I = Y\sigma\sqrt{(\pi\sqrt{area})} \quad (1)$$

proposed by Murakami (2002), where $\sqrt{area}$ represents the killer defect size evaluated by image analysis on SEM fractographies, σ represent the tensile stress at fracture and Y is a dimensionless coefficient representative of defect position (0.65 for surface defects, 0.5 for internal ones). Figure 8 summarizes and compares size $\sqrt{area}$ and stress intensity factor K_I for killer defects of CHT and HPHT samples. Despite the large scatter, killer defects exhibited a similar size (156±79 µm for CHT samples, 148±42 µm for HPHT ones) and stress intensity factor K_I (32.2±11 MPa·m$^{1/2}$ for CHT samples and 32.8±4 MPa·m$^{1/2}$ for HPHT ones) in both heat treatment conditions. Note that the stress intensity factor K_I was extremely close to the fracture toughness K_{IC} of the ESR-produced steel reported by

Ceschini et al. (2018) (33±1.1 MPa·m$^{1/2}$, red dotted line in Figure 8-b). Therefore, it can be concluded that tensile fracture of LPBF samples occurred via unstable crack propagation from a large discontinuity, that acted as killer defect and for which it was verified the critical condition $K_I = K_{IC}$. Moreover, no significant difference in killer defects size existed between samples subjected to CHT and HPHT treatment. By analysing at higher magnification killer defects in Figure 7, it can be seen that in CHT specimens (Figure 9-a) tensile fractures originated from large discontinuities consistent with *Lack of Fusion* defects resulting from the LPBF process in view of their large size, complex shape and surface morphology (Mostafaei et al. (2022)). SEM-EDS analyses indicated a localized enrichment of O, Si, Mn, Cr and V on the surface of *Lack of Fusion* defects due to the presence of µm-size oxides, consistent with the typical non-metallic inclusions found in steels and resulting from their production route. Killer defects at the crack initiation sites of HPHT specimens (Figure 9-b) exhibited size, shape and O, Si, Mn, Cr and V enrichment similar to *Lack of Fusion* defects in CHT ones, but a significant lower volume (due to the lower depth along the normal direction to the fracture surface), appearing as *crack-like* flat defects, and a different surface morphology at high magnification. In fact, they did not exhibit the surface appearance of *Lack of Fusion* defects, resulting from steel solidification during LPBF, but sub-µm dimples containing small particles and larger regions consistent with the oxides found on *Lack of Fusion* defects in CHT samples. While it is clear that killer *Lack of Fusion* defects in CHT samples existed before tensile tests (created during the LPBF process), the presence of dimples indicates that the surface of killer defects in HPHT samples was created via *micro-voids nucleation and coalescence* under an applied load (i.e., during tensile tests), possibly from a pre-existing defect or discontinuity.

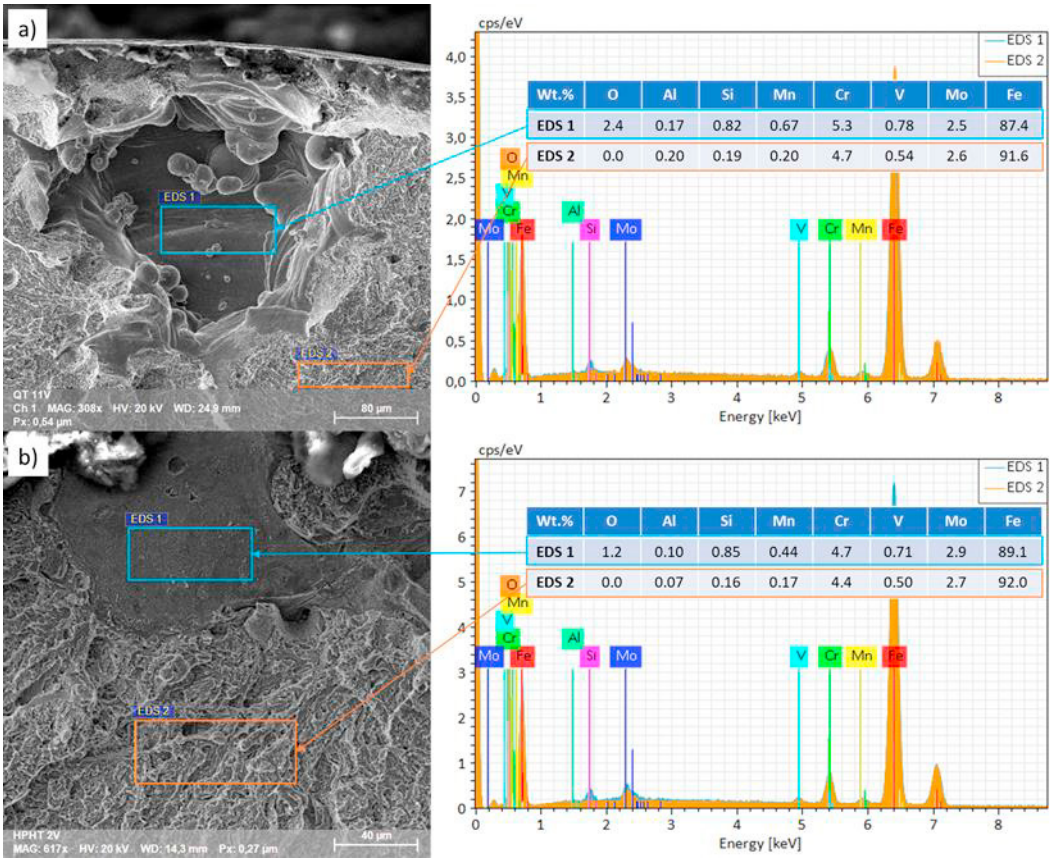

Fig. 7. Killer defects at crack initiation sites in CHT (a) and HPHT (b) samples and SEM-EDS analyses showing the local enrichment of Cr, V, Mn, Si and O.

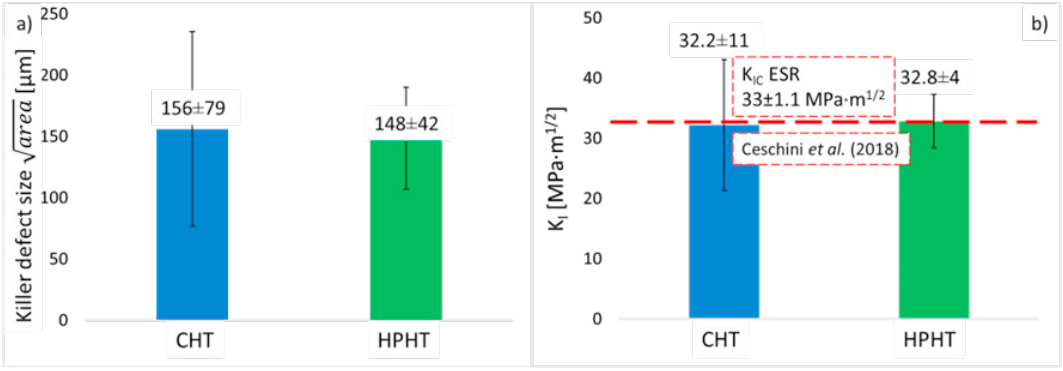

Fig. 8. Comparison of size $\sqrt{area}$ (a) and stress intensity factor K_I (b) of the *killer* defect observed at the crack initiation site in CHT and HPHT samples (the red dotted line indicates the steel fracture toughness K_{IC} reported by Ceschini et al. (2018)).

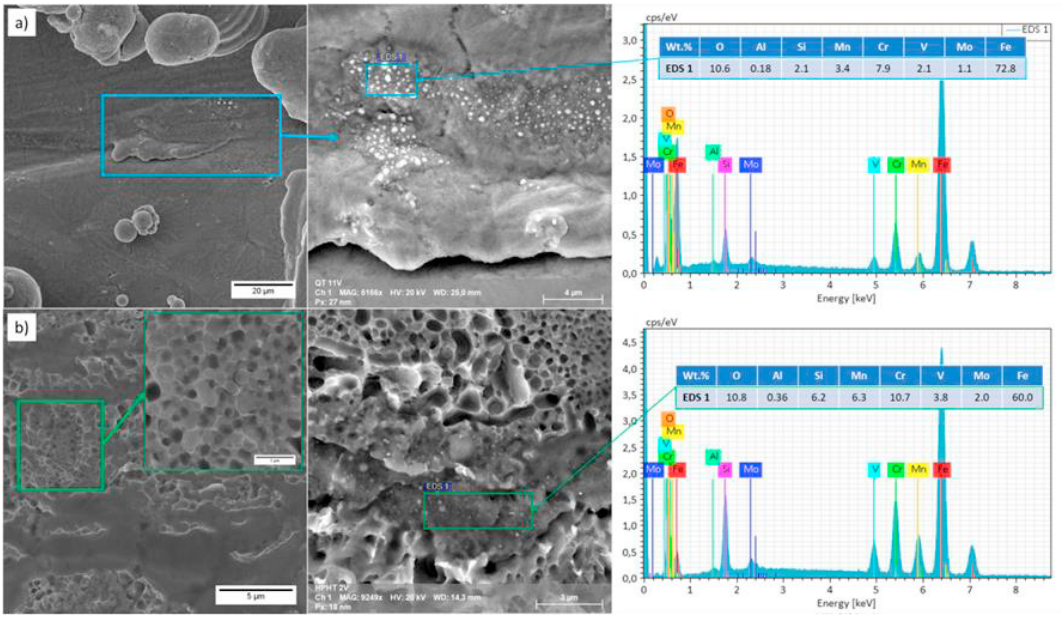

Fig. 9. High magnification SEM images SEM-EDS analyses of the surface of *killer* defects in CHT (a) and HPHT (b) samples, showing the presence of Si, Mn, Cr, Al and V rich oxides. Note the presence of dimples on *killer* defects in HPHT samples.

As shown in Figure 11-a, oxide-containing *Lack of Fusion* defects were also found on polished metallographic sections. Yang et al. (2021), Liverani et al. (2020) and Yan et al. (2018) described the formation of SiO_2, $(Mn,Cr)Cr_2O_4$ spinel, $MnSiO_3$ rhodonite, and in general Si, Cr and Mn based oxides, during the LPBF solidification of AISI 316L stainless steel as a result of the in-situ reaction between molten steel and O pick-up from the build chamber atmosphere and/or from the feedstock powder. Moreover, Liverani et al. (2020) reported the formation of non-metallic inclusions ($(Mn,Fe)_2SiO_4$ olivine) in AISI 316L samples manufactured via LPBF during the subsequent HIP and/or high temperature solution annealing. Defects found in HPHT samples, reported in Figure 11-b, exhibited a complex shape consistent with *Lack of Fusion* defects, but a narrow, *crack-like* appearance. While *Lack of Fusion* defects in CHT samples possessed a certain volume, probably filled the inert gas present in the building chamber during LPBF, the small, extremely narrow volume of defects in HPHT samples was entirely filled with oxides.

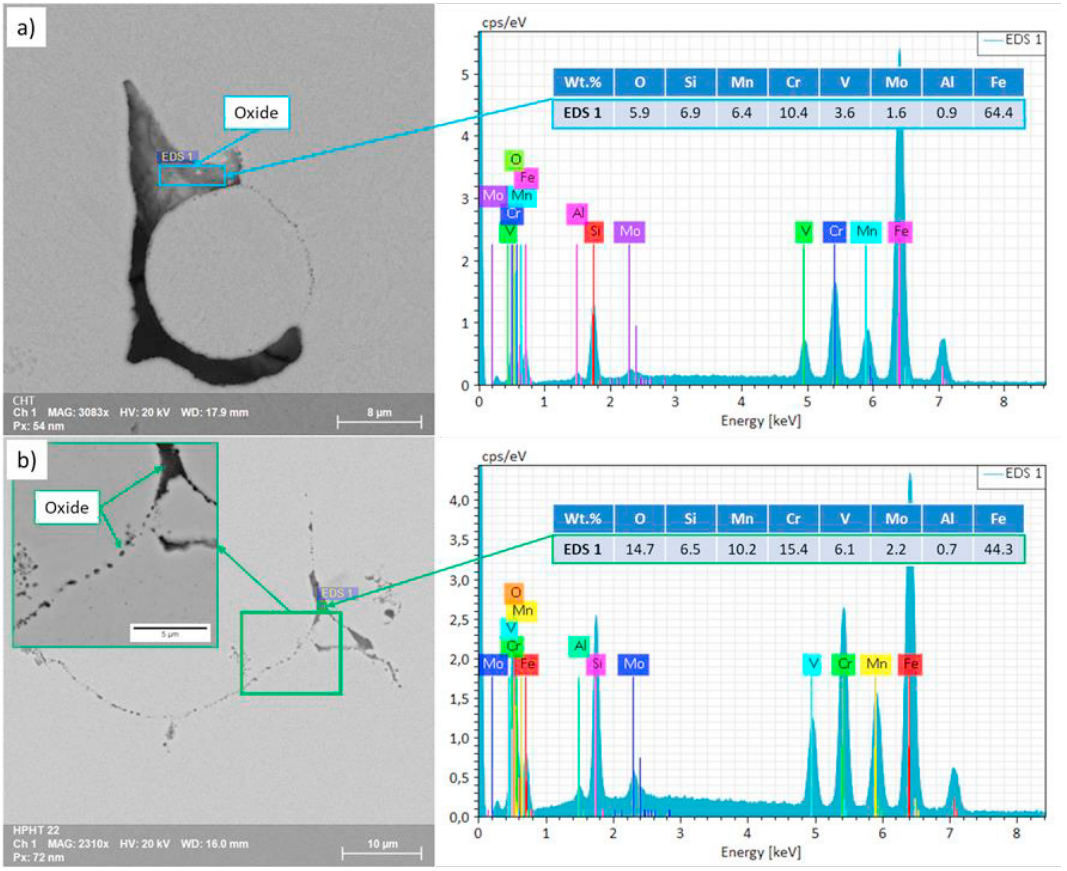

Fig. 10. Examples of defects found on metallographic sections: *Lack of Fusion* in a CHT sample (a) and shrunk *Lack of Fusion* filled with oxides in a HPHT sample (b).

Following the characteristics of defects observed on metallographic sections and at the crack initiation sites of tensile specimens, it is proposed that the discontinuities which acted as killer defects in HPHT samples (as well as defects such as the one reported in Figure 11-b) originated from previous oxide-containing *Lack of Fusion* defects from the LPBF process (which are responsible for the tensile failure of CHT specimens), severely modified but not effectively eliminated by the HIP+austenitizing step (i). The effect of the HIP+austenitizing step of HPHT on oxide-containing *Lack of Fusion* defects schematically depicted in Figure 13. In particular, defects shrink via plastic flow under the high pressure applied at high temperature during step (i) of HPHT (HIP+austenitizing step), leading to higher density and lower defect content of HPHT samples compared to CHT ones. However, the presence of oxides on the inner surfaces of *Lack of Fusion* defects, probably formed during the LPBF solidification and/or coming from the feedstock powder, hinders the formation of an effective metal-to-metal junction between the facing surfaces by acting as an intermediate non-metallic layer. In fact, according to the existing literature data on diffusion bonding, sintering and hot isostatic pressing (German (2014), Shirzadi et al. (2001), Takahashi et al. (1992), Xie et al. (2003)), the presence of a oxide film on metal surfaces hinder the formation of an effective metal-to-metal bond, requiring the additional break-up of the oxide layer and its dissolution through the metal lattice. The effectiveness of HIP in creating a strong metallurgical bond in presence of oxide layers depends on the maximum oxygen solubility in the base metal and on the equilibrium constant K_{eq} of the metal-oxygen reaction. For example, Ti has high O_2 solubility and K_{eq} constant, therefore it can easily dissolve oxide films and form effective metallurgical bonds during HIP. On the opposite, the dissolution of oxide films on iron and steels requires longer times, due to the considerably lower solubility of O_2 in Fe and K_{eq}. However, these considerations only refer to base metal oxide films (for example TiO_2 films in Ti alloys, Fe_2O_3 in steels). No indication on the dissolution of complex oxides, containing Si, Mn, Cr,

V and Al, in iron and steels was found in the literature. As a result of this incomplete junction, narrow defects with size and shape similar to the original *Lack of Fusion* but with lower depth and entirely filled with oxides, such as the one showed in Figure 11-b, remain in the material after HPHT. Considering their formation mechanism, oxide-filled defects found in HPHT samples can be indicated as *Incomplete Junction* defects, in analogy to *Lack of Fusion* ones.

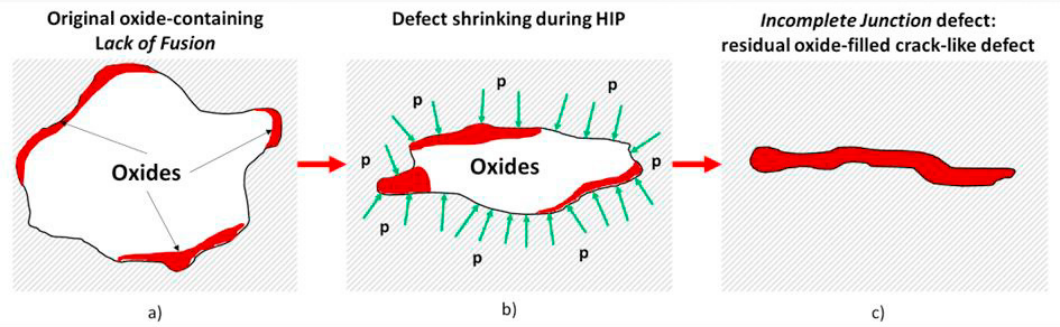

Fig. 11. Effect of HIP+austenitizing (step (i) of HPHT) on oxide-containing *Lack of Fusion* defects: original defect (a), defect shrinking via plastic flow (b), residual oxide-filled *Incomplete Junction* defect (c).

Figure 12 depicts the behaviour of *Lack of Fusion* and *Incomplete Junction* defects during tensile tests. In CHT specimens (Figure 12-a), *Lack of Fusion* defects directly acted as *killer* defects causing unstable crack propagation at $K_I = K_{IC}$, thus leading to specimen failure. Instead, no *volumetric* discontinuity existed prior to tensile tests in HPHT specimens but narrow, oxide-filled discontinuities, here indicated as *Incomplete Junction* defects, originated from the same *Lack of Fusion* defects as described in Figure 11. It is proposed that, during tensile tests, the internal oxide early fails under the applied load creating the dimples-covered discontinuity observed on the fracture surface (with size and shape of the original *Lack of Fusion*), which then acted as killer defect at the critical condition $K_I = K_{IC}$. Since the mechanism described in Figure 11 did not affect appreciably the size of original Lack of Fusion defects, as testified by the comparable size of *killer* defects on the fracture surfaces of CHT and HPHT samples (Figure 4), HPHT did not result in a significant increase of tensile strength.

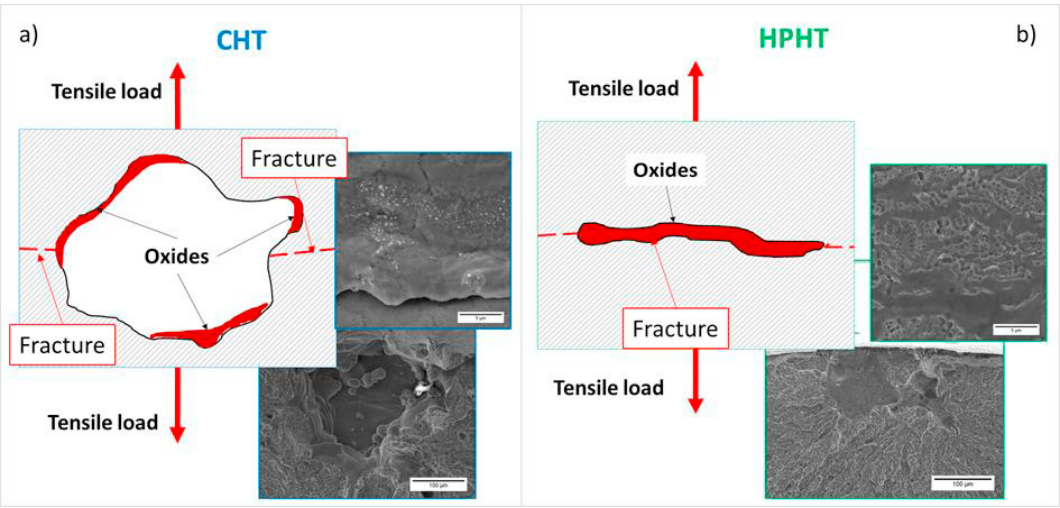

Fig. 12. Schematic representation of the behaviour of defects during tensile tests: *Lack of Fusion* defect in a CHT sample, acting as *killer* defect (a); formation of the dimples-covered discontinuity from an *Incomplete Junction* defect in a HPHT sample, which then acted as *killer* defect (b).

The proposed effect of HIP+austenitizing on *Lack of Fusion* defects (Figure 11) and mechanism of *killer* defects formation (Figure 12) in HPHT samples, related to the above discussed *Incomplete Junction* defects, explains the same tensile failure mechanism and strength among CHT and HPHT specimens, but it does not justify the dramatical loss of ductility of HPHT specimens. As can be noted in Figure 13, both CHT and HPHT treatments resulted in a tempered martensite microstructure, with no evidence of the typical hierarchical structure of LPBF parts featuring melt pools, oriented columnar grains and a cellular solidification sub-structure, as a consequence of the austenitizing step of heat treatment cycles. However, while CHT samples exhibited a homogeneous prior austenite grain (PAG) size of approximatively 5-10 μm, HPHT samples featured a non-uniform PAG size, with regions of severe grain coarsening in a globally fine microstructure. These coarsened grains may explain the reduced ductility of HPHT samples and are likely to be caused by the higher duration of step (i) in HPHT compared to the CHT treatment. No other microstructural difference was observed between CHT and HPHT samples.

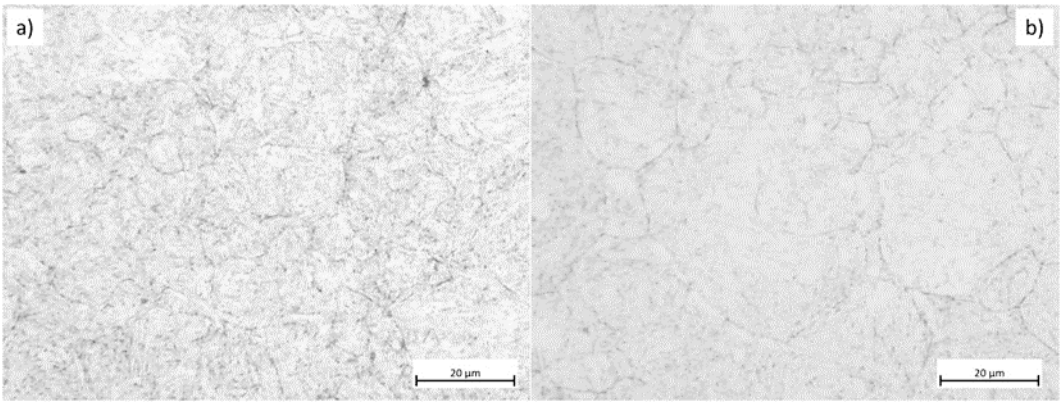

Fig. 13. Microstructure of CHT (a) and HPHT (b) samples.

4. Conclusions

In the present work, the effect of an innovative *high pressure heat treatment* (HPHT) on the tensile properties of a hot work tool steel manufactured via LPBF was investigated. HPHT was designed to integrate the quenching and multiple tempering heat treatment and hot isostatic pressing (HIP) in a single treatment, to simultaneously reduce number and size of internal LPBF defects and to obtain high hardness and mechanical properties. For comparison, the microstructure and mechanical properties of samples subjected to the conventional quenching and tempering treatment performed in vacuum (indicated as CHT) were evaluated. The following conclusions can be drawn:

- HPHT led to significant material densification by reducing the number and size of LPBF defects, resulting in near-full-density samples. *Lack of Fusion* defects were shrunk, with consequent volume reduction, but not effectively eliminated due to the presence of oxides on the inner surfaces, which hindered the formation of metal-to-metal junctions thus leading to residual *Incomplete Junction* defects.
- Compared to the conventional CHT treatment, HPHT led to negligible hardness, proof and tensile strength variations, but a significant reduction of ductility (approximatively -50%). The loss of ductility for HPHT samples was attributed to the non-homogeneous microstructure with coarsened grains, probably resulting from the longer austenitizing step compared to CHT to promote material densification.
- Tensile fracture occurred via unstable crack propagation from large discontinuities in both CHT and HPHT samples when the stress intensity factor K_I reached the steel fracture toughness K_{IC}.
- In CHT samples, large *Lack of Fusion* defects resulting from LPBF acted as *killer* defects.
- In HPHT samples, the oxide inside *Incomplete Junction* defects early failed during the tensile test, creating a dimples-covered discontinuity with size of the original *Lack of Fusion* which then acted as killer defect.

References

Ahlfors, M., 2020. Hot Isostatic Pressing for Metal Additive Manufacturing. In: Bourell, D.L., Frazier, W., Kuhn, H., Seifi, M. (Eds.), ASM Handbook, Vol 24, Additive Manufacturing Processes. ASM International, pp. 316–323. https://doi.org/10.31399/asm.hb.v24.a0006552.

Åsberg, M., Fredriksson, G., Hatami, S., Fredriksson, W., Krakhmalev, P., 2019. Influence of post treatment on microstructure, porosity and mechanical properties of additive manufactured H13 tool steel. Materials Science and Engineering: A 742, 584–589. https://doi.org/10.1016/j.msea.2018.08.046.

Atkinson, H.V., Davies, S., 2000. Fundamental aspects of hot isostatic pressing: An overview. Metallurgical and Materials Transactions A 31, 2981–3000. https://doi.org/10.1007/s11661-000-0078-2.

Baldissera, P., Delprete, C., 2008. Deep Cryogenic Treatment: A Bibliographic Review. The Open Mechanical Engineering Journal 2, 1-11. https://doi.org/10.2174/1874155X00802010001.

Cegan, T., Pagac, M., Jurica, J., Skotnicova, K., Hajnys, J., Horsak, L., Soucek, K., Krpec, P., 2020. Effect of Hot Isostatic Pressing on Porosity and Mechanical Properties of 316 L Stainless Steel Prepared by the Selective Laser Melting Method. Materials 13, 4377. https://doi.org/10.3390/ma13194377.

Ceschini, L., Morri, A., Morri, A., Messieri, S., 2018. Replacement of Nitrided 33CrMoV Steel with ESR Hot Work Tool Steels for Motorsport Applications: Microstructural and Fatigue Characterization. Journal of Materials Engineering and Performance 27, 3920-3931. https://doi.org/10.1007/s11665-018-3481-9.

DebRoy, T., Wei, H.L., Zuback, J.S., Mukherjee, T., Elmer, J.W., Milewsi, J.O., Beese, A.M., Wilson-Heid, A., De, A., Zhang, W., 2018. Additive manufacturing of metallic components – Process, structure and properties. Progress in Materials Science 92, 112-224. https://doi.org/10.1016/j.pmatsci.2017.10.001.

Du Plessis, A., Macdonald, E., 2020. Hot isostatic pressing in metal additive manufacturing: X-ray tomography reveals details of pore closure. Additive Manufacturing 34, 101191. https://doi.org/10.1016/j.addma.2020.101191.

Du Plessis, A., Yadroitsava, I., Yadroitsev, I., 2020. Effects of defects on mechanical properties in metal additive manufacturing: A review focusing on X-ray tomography insights. Materials & Design 187, 108385. https://doi.org/10.1016/j.matdes.2019.108385.

German, M.R., 2014. Sintering: from Empirical Observations to Scientific Principles. Elsevier. https://doi.org/10.1016/C2012-0-00717-X.

Hebert, R.J., 2016. Viewpoint: metallurgical aspects of powder bed metal additive manufacturing. Journal of Materials Science 51, 1165-1175. https://doi.org/10.1007/s10853-015-9479-x.

Krakhmalev, P., Fredriksson, G., Thuvander, M., Åsberg, M., Vilardell, A.M., Oikonomou, C., Maistro, G., Medvedeva, A., Kazantseva, N., 2020. Influence of heat treatment under hot isostatic pressing (HIP) on microstructure of intermetallic-reinforced tool steel manufactured by laser powder bed fusion. Materials Science and Engineering: A 772, 138699. https://doi.org/10.1016/j.msea.2019.138699.

Lee, J., Choe, J., Park, J., Yu, J.-H., Kim, S., Jung, I.D., Sung, H., 2019. Microstructural effects on the tensile and fracture behavior of selective laser melted H13 tool steel under varying conditions. Materials Characterization 155, 109817. https://doi.org/10.1016/j.matchar.2019.109817.

Liverani, E., Lutey, A.H.A., Ascari, A., Fortunato, A., 2020. The effects of hot isostatic pressing (HIP) and solubilization heat treatment on the density, mechanical properties, and microstructure of austenitic stainless steel parts produced by selective laser melting (SLM). The International Journal of Advanced Manufacturing Technology 107, 109–122. https://doi.org/10.1007/s00170-020-05072-9.

Maistro, G., Oikonomou, C., Hosseini, S.B., Brorson, S., 2021. Quenching and Hot Isostatic Pressing of Additively Manufactured Tool Steel. SSRN Electronic Journal. https://doi.org/10.2139/ssrn.3785874.

McGarry, D., 2021. Mechanisms and Appearances of Ductile and Brittle Fracture in Metals. In: Miller, B.A., Shipley, R.J., Parrington, R.J., Dennies, D.P. (Eds.), ASM Handbook, Vol. 11, Failure Analysis and Prevention. ASM International, pp. 304–342. https://doi.org/10.31399/asm.hb.v11.a0006775.

Mostafaei, A., Zhao, C., He, Y., Reza Ghiaasiaan, S., Shi, B., Shao, S., Shamsaei, N., Wu, Z., Kouraytem, N., Sun, T., Pauza, J., Gordon, J.V., Webler, B., Parab, N.D., Asherloo, M., Guo, Q., Chen, L., Rollett, A.D., 2022. Defects and anomalies in powder bed fusion metal additive manufacturing. Current Opinion in Solid State and Materials Science 26, 100974. https://doi.org/10.1016/j.cossms.2021.100974.

Murakami, Y., 2019. Stress concentration In: Metal Fatigue (Second Edition) Effects of Small Defects and Nonmetallic Inclusions. Elsevier, pp.13-27. https://doi.org/10.1016/B978-0-12-813876-2.00002-9.

Parrington, R.J., 2021. Fatigue Fracture Appearances. In: Miller, B.A., Shipley, R.J., Parrington, R.J., Dennies, D.P. (Eds.), ASM Handbook, Vol 11, Failure Analysis and Prevention. ASM International, pp. 343-355. https://doi.org/10.31399/asm.hb.v11.a0006776.

Qin, S., Herzog, S., Kaletsch, A., Broeckmann, C., 2021. Effects of Pressure on Microstructure and Residual Stresses during Hot Isostatic Pressing Post Treatment of AISI M50 Produced by Laser Powder-Bed Fusion. Metals 11, 596. https://doi.org/10.3390/met11040596.

Shirzadi, A.A., Assadi, H., Wallach, E.R., 2001. Interface evolution and bond strength when diffusion bonding materials with stable oxide films. Surface and Interface Analysis 31, 609–618. https://doi.org/10.1002/sia.1088.

Sridar, S., Zhao, Y., Li, K., Wang, X., Xiong, W., 2020. Post-heat treatment design for high-strength low-alloy steels processed by laser powder bed fusion. Materials Science and Engineering: A 788, 139531. https://doi.org/10.1016/j.msea.2020.139531.

Takahashi, Y., Nakamura, T., Nishiguchi, K., 1992. Dissolution process of surface oxide film during diffusion bonding of metals. Journal of Materials Science 27, 485–498. https://doi.org/10.1007/BF00543942.

Tocci, M., Pola, A., Gelfi, M., La Vecchia, G.M., 2020. Effect of a New High-Pressure Heat Treatment on Additively Manufactured AlSi10Mg Alloy. Metallurgical and Materials Transactions A 51, 4799–4811. https://doi.org/10.1007/s11661-020-05905-y.

Vilardell, A.M., Hosseini, S.B., Åsberg, M., Dahl-Jendelin, A., Krakhmalev, P., Oikonomou, C., Hatami, S., 2021. Evaluation of post-treatments of novel hot-work tool steel manufactured by laser powder bed fusion for aluminum die casting applications. Materials Science and Engineering: A 800, 140305. https://doi.org/10.1016/j.msea.2020.140305.

Xie, G., Ohashi, O., Song, M., Furuya, K., Noda, T., 2003. Behavior of oxide film at the interface between particles in sintered Al powders by pulse electric-current sintering. Metallurgical and Materials Transactions A 34, 699–703. https://doi.org/10.1007/s11661-003-0104-2.

Yang, X., Tang, F., Hao, X., Li, Z., 2021. Oxide Evolution During the Solidification of 316L Stainless Steel from Additive Manufacturing Powders with Different Oxygen Contents. Metallurgical and Materials Transactions B 52, 2253–2262. https://doi.org/10.1007/s11663-021 02191-w.